JACS Au
AN OPEN ACCESS JOURNAL OF THE AMERICAN CHEMICAL SOCIETY

pubs.acs.org/jacsau

Article

Microcurvature Controllable Metal–Organic Framework Nanoagents Capable of Ice-Lattice Matching for Cellular Cryopreservation

Nayeong Jeon, In-ho Jeong, Eunyeong Cho, Ilhyung Choi, Jiyeon Lee, Eun Hee Han, Hee Jung Lee,* Peter C.W. Lee,* and Eunji Lee*

Cite This: *JACS Au* 2023, 3, 154–164

Read Online

ACCESS | Metrics & More | Article Recommendations | Supporting Information

ABSTRACT: Ice-binding proteins (IBPs) produced by psychrophilic organisms to adapt for the survival of psychrophiles in subzero conditions have received illustrious interest as a cryopreservation agent required for cells and tissues to completely recover after freezing/thawing. Depressing water-freezing point and avoiding ice-crystal growth affect their activities which are closely related to the presence of ice crystal well-matched binding moiety. The interaction of IBPs with ice and water is critical in enhancing their freeze avoidance against cell or tissue damage. Metal–organic frameworks (MOFs) with a controllable lattice at the molecular level and a size at the nanometer scale can offer periodically ordered ice-binding sites by modifying organic linkers and controlling microcurvature at the ice surface. Herein, zirconium (Zr)-based MOF-801 nanoparticles (NPs) with good biocompatibility were used as a cryoprotectant that is well dispersed and colloidal-stable in an aqueous solution. The MOF NP size was precisely controlled, and 10, 35, 100, and 250 nm NPs were prepared. The specific IBPs-mimicking pendants (valine and threonine) were simply introduced into the MOF NP-surface through the acrylate-based functionalization to endow with hydrophilic and hydrophobic dualities. When small-sized MOF-801 NPs were attached to ice, they confined ice growth in high curvature between the adsorption sites because of the decreased radius of the convex area of the growth region, leading to highly enhanced ice recrystallization inhibition (IRI). Surface-functionalized MOF NPs could increase the number of anchored clathrate water molecules with hydrophilic/hydrophobic balance of the ice-binding moiety, effectively inhibiting ice growth. The MOF-801 NPs were biocompatible with various cell lines regardless of concentration or NP surface-functionalization, whereas the smaller-sized surface-functionalized NPs showed a good cell recovery rate after freezing/thawing by induction of IRI. This study provides a strategy for the fabrication of low-cost, high-volume antifreeze nanoagents that can extend useful applications to organ transplantation, cord blood storage, and vaccines/drugs.

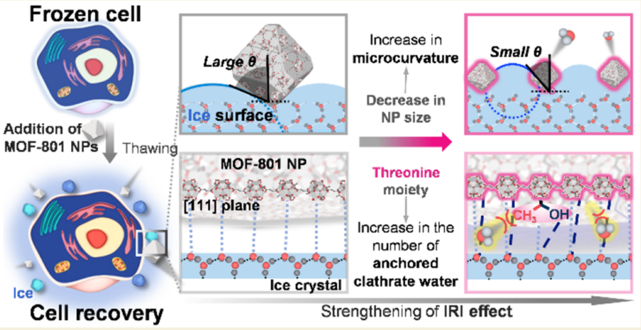

KEYWORDS: *Metal–organic framework nanoparticles, Microcurvature control, Ice-binding motifs, Ice recrystallization inhibitors, Cryoprotectants*

INTRODUCTION

Owing to their binding ability with ice surfaces to either inhibit or promote ice growth,[1,2] ice-binding proteins (IBPs) are considered auspicious material candidates for the storage and transport of drugs, cells, tissues, and foods. As such, they offer great prospects in the biochemical,[3] pharmaceutical,[4,5] and food industries,[6] e.g., in tissue engineering, gene therapy, therapeutic protein production, and transplantation. Understanding the correlation between the IBP architecture and its function, based on the ice chemistry, inspires the rational design of cell cryopreservatives.[7,8] Natural IBPs exhibit periodic spacing of an ice-interactable moieties, similar to the spacing of ice crystal lattice, which enables them to be well adsorbed to the ice surface and induces microcurvature of the ice surface.[9−11] Therefore, for the development of the cryopreservation agent with high freeze-avoidance activity, the assembled structures of natural IBPs are as or more important as the amino acid sequence similarity of natural IBPs. Their cryopreservation activity is determined by thermal hysteresis (TH)[12,13] and ice recrystallization inhibition (IRI) effects.[13−16] Considering that IBPs are costly to extract and

Received: October 11, 2022
Revised: December 6, 2022
Accepted: December 7, 2022
Published: December 20, 2022

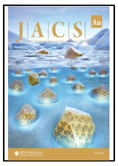

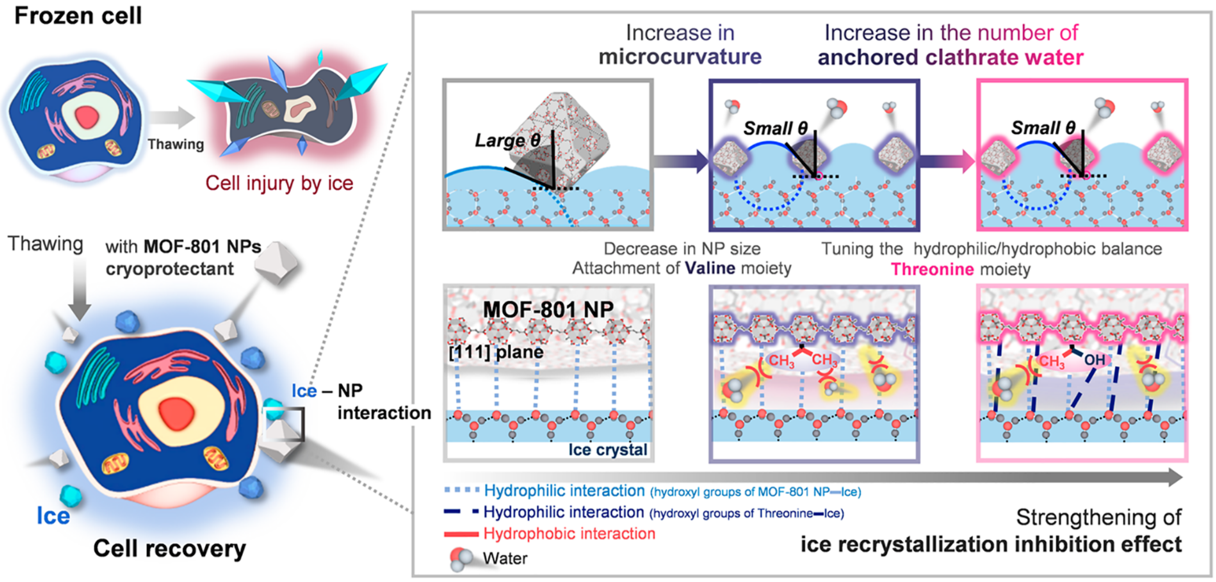

Figure 1. Schematic illustration of (left) the use of MOF-801 NPs as a cryoprotectant for preventing cell injury caused by ice crystal growth during cell freezing and thawing, and (right) ice recrystallization inhibition effect of MOF-801 NPs by controlling the NP size and introducing ice-binding amino acids that affect the microcurvature on the ice surface. The anchored water molecules allow the MOF-801 NPs to adsorb well to certain ice planes.

lead to irreversible denaturation, water-miscible chemical agents, such as dimethyl sulfoxide (DMSO) and sodium phosphate, were used for cell cryopreservation.[17,18] However, while the cell recovery rate of these chemicals is relatively high, their biocompatibility above a certain concentration severely diminishes,[19,20] resulting in phenotypic alterations and changes in the DNA methylation profiles of cells after repeated freezing/thawing cycles.[21,22] Efforts to obviate these limitations have led to a variety of molecular design strategies to construct synthetic polymers or biomolecules that mimic natural IBPs, particularly antifreeze proteins (AFPs), thermal hysteresis proteins (THFPs), and ice-recrystallization inhibition proteins (IRIPs).[23−26] However, these substances are very arduous and complex to control a regular structural organization at the molecular level due to their high thermodynamic degrees of freedom and require multistage synthetic processes.

Meanwhile, metal−organic framework (MOF) nanoparticles (NPs) with a porous crystalline structure, their chemical functions, and particle sizes can be precisely controlled,[27,28] enabling their utilization in water harvesting,[29,30] electrochemical devices,[31,32] gas separation,[33] catalysts,[34] and biomedical applications.[35] Such MOF NPs can be a promising nanoscaffold that is capable of adopting the natural characteristics of IBPs, including the regular configuration and location of functional moieties affecting ice nucleation and growth at the molecular scale. Zhu et al. reported of zirconium (Zr)-based UiO-66 MOF NPs that can regularly arrange hydrogen donors to match and bind to the ice crystal plane, can be used as an effective cryopreservative for red blood cells.[36] Zr-based MOFs exhibit excellent water dispersibility, colloidal stability, and biocompatibility, rendering them promising eco-friendly materials for cryopreservation. However, the effect of the MOF NP size on the curvature at the ice−water interface, as well as the ice nucleation and growth rate, has yet to be investigated. This study provides a useful strategy for strengthening and optimizing the cell and tissue preservation performance of MOF NPs even with the same configuration.

The precise size-control of the Zr-based MOF NPs and their internal periodic ice-interactive functional residues could provide insight regarding the lowering of the freezing temperature by the Gibbs−Thomson effect,[9] as well as the effect on the curvature change at the ice−water interface of the solid−liquid equilibrium. The attachment of IBP-derived antifreeze moieties to the MOF could enhance their strong adherence to ice on one side and effectively block access to water on the other, thereby inhibiting successive ice growth. In particular, the curved interface created by NPs lowers the temperature at which ice propagates through a confined space, thereby highlighting the applicability of MOF NPs as a cryopreservative for cells and tissues.

In this context, we prepared MOF-801 NPs comprising hydrogen donor groups that facilitate the formation of hydrogen bonds between adjacent water molecules according to the MOF NP-size (Figure 1). The small NPs provided positive interfacial energy by inducing a local high curvature at the equilibrium points. Furthermore, the introduction of a long-range arrangement of ice-binding residues regulated the ice growth between the ice surface-bound MOFs, maximizing the IRI rate during the freezing/thawing process and thereby amplifying the cell-cryoprotective effects by avoiding cell injury and death. To emulate natural AFP, valine (Val) and threonine (Thr), two amino acids acting as ice-binding moieties,[11] were incorporated into the surface of the MOF-801 NPs, further strengthening the IRI effects.

■ RESULTS AND DISCUSSION

Preparation of MOF-801 NPs with Different Sizes

The first attempt was to prepare the nanoporous MOF-801 NPs with different NP sizes (10, 35, 100, and 250 nm), from the $Zr_6O_4(OH)_4(fumarate)_6$ secondary building units[37] through solvothermal reactions, where the mixed solution containing Zr salts, fumaric acid of organic linkers, and modulating agents were heated for a certain time (Figure 2A, see the Supporting Information). The NP size was precisely

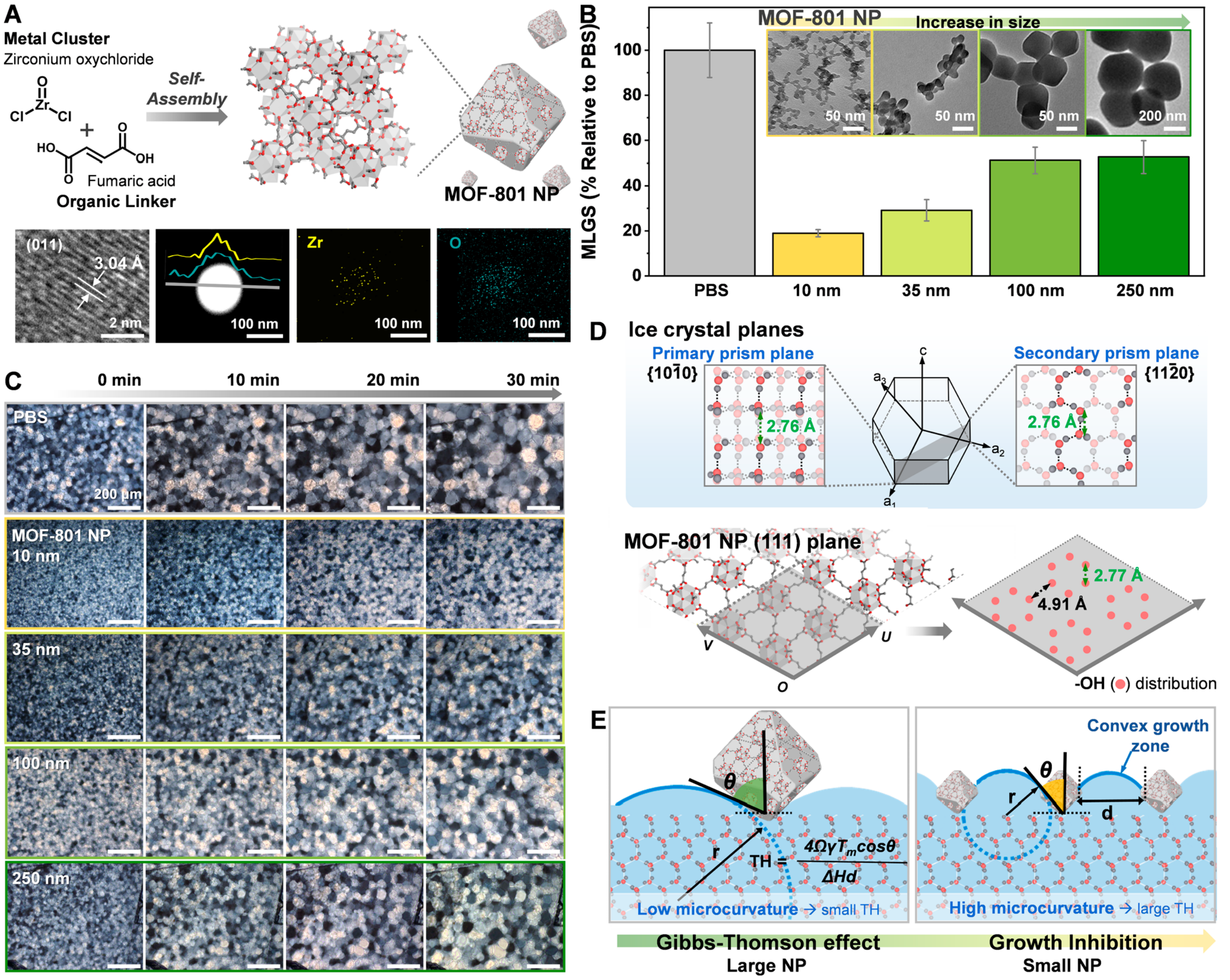

Figure 2. (A) Schematic illustration of the solvothermal synthesis of MOF-801 NP. Insets are, in respective order: HRTEM image of the lattice fringes of the (011) plane of MOF-801 NP; STEM and EDS elemental mapping images with line scan patterns of the MOF-801 NP (100 nm) with the corresponding Zr and O elemental mappings. (B) Quantitative assessment of IRI activity of MOF-801 NPs with various sizes (10, 35, 100, and 250 nm in 0.5 mg/mL of PBS solution) calculated from Figure 2C after ice crystals were annealed for 30 min at −6 °C. MLGS = mean largest grain size relative to PBS negative control. Error bars represent the standard deviation from three individual experiments. Insets are TEM images of MOF-801 NPs of different sizes. (C) Cryomicroscopy images showing inhibition of ice crystal growth by adding MOF-801 NPs of various sizes. Images were taken with 10 min intervals. (D) Schematic diagram of hexagonal ice crystal planes (primary and secondary prism planes). (111) plane and corresponding hydroxyl group spacing and distribution diagram of MOF-801 NP. The hydroxyl spacing of the ice crystals and MOF-801 NP (111) planes with good matching are indicated by green arrows and letters. (E) Schematic illustration for the comparison of the local ice surface microcurvature upon binding by small and large MOF-801 NPs. The blue bold line indicates the local curvature that occurs after the MOF NP adheres to the ice surface (*r*: radius of the convex ice interface, *d*: MOF-801 NP spacing, and *θ*: contact angle between the ice surface curvature and the MOF-801 NP).

controlled by tuning the nucleation stage using the following method and was confirmed by transmission electron microscopy (TEM) analysis (insets of Figures 2B and S1A–D). MOF NPs of a specific size were synthesized by controlling the concentration of Zr ions and organic ligands. The length of the diffusion path of the Zr ions was maximized under dilute conditions to form small MOF-801 NPs. On the other hand, concentrated conditions provided large MOF NPs. The Zr-based MOFs ensure exceptional stability and topological diversity, and water-soluble MOF-801 shows a 3D structure based on face-cubic centered (fcu) topology.[38,39] The synthesized MOF-801 NPs with various sizes were examined by Fourier-transform infrared (FT-IR) spectroscopy (Figure S2). The asymmetric stretching vibration peak located at 1575 cm^{-1} from −COO− appeared along with the shift of the symmetric stretching vibration peak at 1400 cm^{-1} originated from the fumaric acid, verifying the formation of MOF-801 NP.[40] The spectrum of the fumaric acid only showed the symmetric stretching peak of −COO− at 1450 cm^{-1}. The C═O stretching vibration peak, corresponding to the carboxylic group from the fumaric acid, was confirmed in the range of 1655−1675 cm^{-1}, showing a slight shift toward lower wavenumber as the NP size increased, caused by bond lengthening.

The phase purity of the MOF NPs was confirmed by powder X-ray diffraction (PXRD) analysis. The diffraction patterns were in agreement with the simulated crystallographic data and standard values (Figure S3). The lattice parameter for the

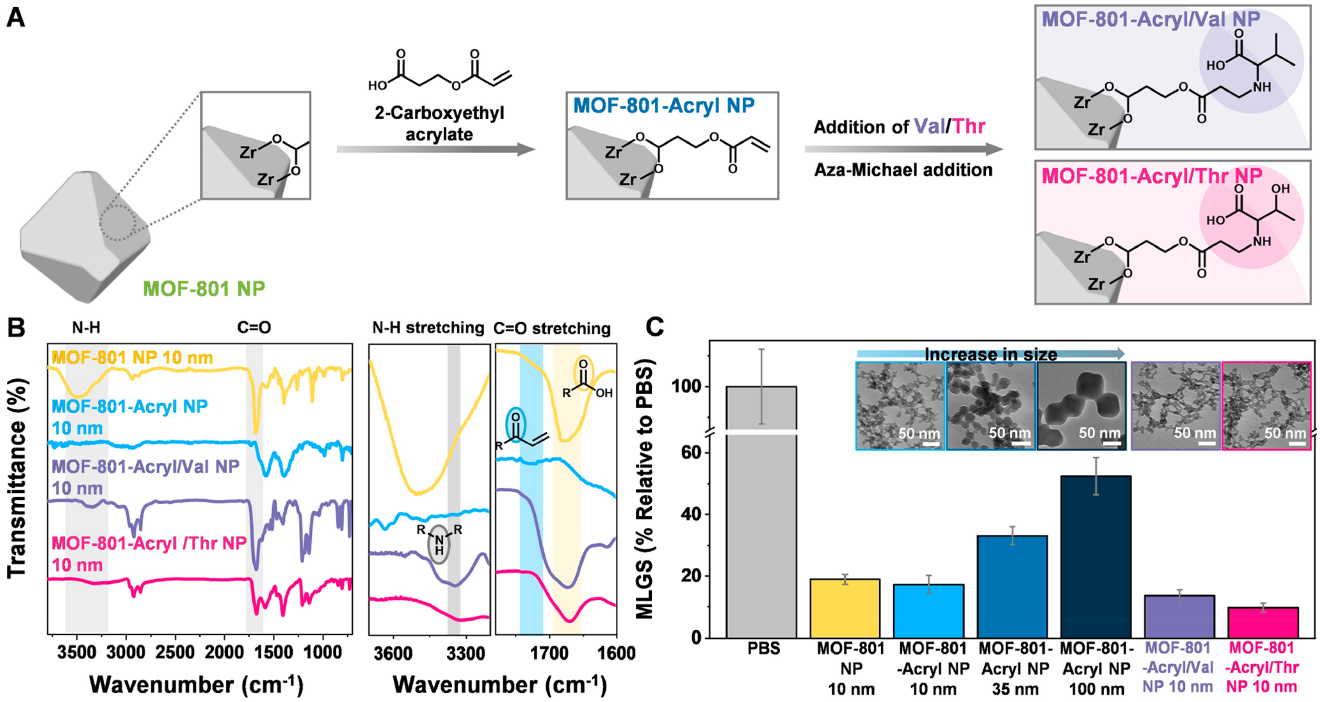

Figure 3. (A) Schematic illustration of the surface-functionalization of MOF-801 NPs. Synthesis of MOF-801-Acryl NPs by 2-carboxyethyl acrylate addition onto the MOF-801 NPs through ligand exchange, and formation of MOF-801-Acryl/Val and MOF-801-Acryl/Thr NPs via the introduction of ice-binding moieties through an aza-Michael addition reaction. (B) Stacked FT-IR spectra of MOF-801 NP 10 nm, MOF-801-Acryl NP 10 nm, MOF-801-Acryl/Val NP 10 nm, and MOF-801-Acryl/Thr NP 10 nm. The enlarged graphs focus on each peak taken from the shadow zones representing the N−H and C=O stretching vibrations, respectively. (C) Quantitative assessment of IRI activity of the surface-functionalized MOF-801 NPs with various sizes (MOF-801-Acryl NPs 10, 35, and 100 nm in 0.5 mg/mL PBS solution) calculated from Figure S10 after ice crystals were annealed for 30 min at −6 °C. The error bars represent the standard deviation from the three individual experiments. Insets from left to right are TEM images of MOF-801-Acryl NP of 10, 35, and 100 nm, MOF-801-Acryl/Val, and/Thr NPs 10 nm from the left, respectively.

synthesized MOF-801 NPs was calculated to be in the range of 17.88 ± 0.05 Å with each size, which is very close to the lattice parameter of 17.91 Å that is known for the bulk material.[37] In addition, crystallite size-related peaks broadening was observed as the size of the MOF-801 NPs became smaller, where an increased NP curvature imposed interlayer ordering constraints.[41] The N_2 adsorption−desorption isotherms showing typical type-1 behavior indicated that the MOF NPs exhibited permanent porosity (Figure S1E−H). The high-resolution TEM (HRTEM) measurement results confirmed that the lattice fringes of MOF-801 NP were 3.04, and 1.80 Å indicative of the (011) and (112) planes of ZrO_2, respectively (inset of Figures 2A and S4A).[42] Scanning TEM (STEM) elemental analysis through energy dispersive spectroscopy (EDS) mapping shows the presence of Zr and O from ZrO_2 and fumarate (insets of Figures 2A and S4B,C).

IRI Activity of Ice-Lattice Matching MOF-801 NPs by Microcurvature Control at the Ice−Water Interface

The IRI capabilities of the synthesized MOF-801 NPs were investigated using a "splat" assay, in which ice grains grew significantly by ice recrystallization, for which rapidly frozen NP dispersions in 1X phosphate-buffered saline (PBS) were annealed at −6 °C for 30 min (Figure 2C).[14−16,26]Figure 2B shows the mean largest grain size (MLGS) of the ice crystal, while quantitatively characterizing the IRI activity of each MOF-801 NP (Table S1). All the MOF-801 NPs had a distinct IRI effect compared to that of PBS solution, and the smaller NPs displayed a superior effect. The addition of 10 nm NPs was confirmed to decrease the MLGS of ice by more than 18.9%, as compared to PBS without NP addition. We hypothesized that the IRI effect appeared in MOF-801 NPs of all sizes because the cavities comprising two tetrahedral and octahedral shapes contributed to the water adsorption sites,[29] while the carboxylic groups localized in high density on the top layer surface of the MOF-801 NPs formed hydrogen bonds, thus inhibiting ice growth by pinning on the ice surface. The interaction between the MOF-801 NPs and the ice crystal planes was assessed by matching the distribution of hydroxyl groups that could be hydrogen bond donors or acceptors on the MOF-801 NP crystal plane and observing the spacing of hydroxyl groups on different ice crystal planes (Figures 2D and S5). The (111) plane of the MOF-801 NPs with a fcu crystal structure had a hexagonal 2D lattice, that allowed hydrogen bond donors/acceptors to be distributed with a relatively high density compared to other crystal planes. The (111) plane also exhibited periodic hydroxyl groups with intervals of 2.77 Å, which was well-matched with the primary and secondary prism planes of ice in which hydroxyl groups were distributed at intervals of 2.76 Å to achieve strong hydrogen bonding with these surfaces can be achieved (Figure S5). Additionally, neighboring carboxylic groups with a spacing of 4.91 Å fit well with the distance of interval hydroxyls in the basal plane (4.51 Å).

As shown in the results, by comparing the MLGS according to the size of the NPs, it was confirmed that the IRI activity was dramatically improved as the size of the MOF-801 NPs decreased due to the Gibbs−Thomson effect,[43,44] which addresses the chemical potential of an interface curvature of the ice−water phase in the solid−liquid equilibrium state (Figure 2E). The limited ice growth between MOF-801 NPs pinned on the ice surface increased the local curvature of ice, reducing the radius of these convex growth regions and making them thermodynamically unstable.[9] The correlation between the surface curvature and the freezing point depression was also due to the Gibbs−Thomson effect (see the Supporting Information).[43] When small MOF-801 NPs were absorbed on the ice surface, the concave growth zone of the ice narrowed, consequently increasing the curvature of the ice surface, and further enhancing the IRI effect. At a given concentration, the smaller-sized MOF-801 NPs could make more interfacial contact with ice than the larger-sized NPs, thereby narrowing the gap between the MOF NPs attached to the ice; thus, the growth of ice was confined to a smaller curvature radius.

Enhanced IRI of Ice-Binding Pendant-Tethered MOF-801 NPs

Subsequently, the surface-functionalization of the MOF-801 NPs was explored to introduce an ice-binding residue, which is one of the main features of determining the IRI behavior of natural AFP, on the surface of MOF-801 NP (Figure 3A). The acrylate group was decorated on the surface of the MOF NPs (hereafter denoted as MOF-801-Acryl NPs) via ligand exchange.[45] Val and Thr, which are known to have a high ice-binding affinity,[11] were immobilized on the surface of MOF-801-Acryl NPs using aza-Michael addition (hereafter denoted as MOF-801-Acryl/Val or/Thr NP; Figure S6).[46] The FT-IR spectroscopy and X-ray photoelectron spectroscopy (XPS) results verified the sequential completion of the reactions. As shown in Figure 3B, compared to bare MOF-801 NPs of 10 nm showing the C═O stretching peak of a carboxyl group at 1675 cm^{-1}, the C═O stretching peak of the carboxyl groups in the MOF-801-Acryl NPs weakened, and the C═O stretching peak from the α,β-unsaturated ester appeared at 1720 cm^{-1}. In the MOF-801-Acryl/Val and/Thr NPs, the C═O stretching peak of α,β-unsaturated ester disappeared, while a C═O stretching peak, derived from the C- terminus of the amino acid appeared at 1670 and 1705 cm^{-1}. In addition, an N−H stretching peak from the secondary amine, derived from the combination of acrylate and amino acids, could be observed at 3320 and 3335 cm^{-1} in the MOF-801-Acryl/Val NPs and/Thr NPs, respectively. The TEM images showed that even after surface-functionalization, the size of MOF NPs remained similar compared to that of bare MOF-801 NPs (inset of Figure 3C). Similarly, Val and Thr were successfully introduced onto the 35 and 100 nm MOF-801-Acryl NPs, respectively, as confirmed by FT-IR spectroscopy (Figure S7). XPS spectra suggest the presence of Zr, C, and O in MOF-801 NPs and MOF-801-Acryl NPs 35 nm (Figure S8). Acrylate functionalization was proved with the relative shift of the Zr 3d peak in the spectrum of MOF-801-Acryl NP 35 nm when compared with that of bare MOF-801 NP with the same size. The almost identical positions of Zr $3d_{3/2}$ and $3d_{5/2}$ in both samples mean that the acrylate group was bonded covalently to the MOF NPs surface, not coordinately.[47] Additionally, the introduction of amino acids was further identified with the appearance of an N 1s peak in the spectra of MOF-801-Acryl/Val and/Thr NPs 35 nm. The absence of unreacted amino acid residues, which are known to affect the IRI,[48] was investigated through PXRD, thermogravimetric analysis (TGA),[37] and ^{1}H nuclear magnetic resonance (^{1}H NMR) spectroscopy[50] (Figures S9−S11).[37,49,50] Val and Thr can form the crystals and show the single-crystal characteristic patterns in PXRD (Figure S9).[49] The surface-functionalized MOF-801 NPs did not show any additional peaks that could be derived from the crystals of free amino acids. The removal of residual amino acids was further confirmed by thermogram and ^{1}H NMR spectral analysis (Figures S10 and S11).

The IRI activity of the surface-modified MOF NPs was investigated by the quantitative MLGS values (Figures 3C and S12). As in the case of comparing the IRI activity of bare MOF-801 NPs according to size (Figure 2B), the MOF-801-Acryl NPs showed a superior IRI effect as the size of the NPs decreased (Figure 3C). When Val and Thr were introduced to MOF-801 NPs 10 nm, the relative MLGS reduced noticeably (28 and 49% for MOF-801-Acryl/Val and/Thr NPs compared to that of the bare NPs, respectively). It is known that the introduction of methyl groups by the addition of amino acid moieties onto the NPs repels the water molecules from approaching the ice surface, but the methyl group alone does not induce the IRI effect.[51] MOF-801-Acrly/Val NPs showed an enhanced IRI activity than that of bare MOF-801 NPs, because the carboxylic acid and secondary amine of Val can form hydrogen bonding with the water molecules,[52,53] and synergistically act with the hydrophobic interaction induced by methyl groups from Val (with two methyl groups). Also, the addition of Thr (with a hydroxyl group and a methyl group) to bare MOF-801 NPs could provide stronger hydrogen bonding than the addition of Val (Figure S13), and simultaneously prevent the assimilation of water molecules with ice, thereby inhibiting the growth of ice more effectively.[51,54] In short, the methyl group of Thr repelled the water molecules and locked them in the layer to prevent further growth into ice through hydrogen bonding with the hydroxyl groups. Given the above, it was experimentally verified that controlled hydrophilic and hydrophobic dualities can efficiently regulate ice growth.

Cell-Permeable, Biocompatible MOF NPs

The cell viability of MOF-801 NPs as cryopreservation agents was first investigated on the human embryonic kidney (293T), nontumorigenic lung bronchial epithelial (BEAS-2B), and lung carcinoma epithelial (A549) cell lines, using a CellTiter-Glo 3D assay (Figure 4). After MOF NPs treatment, no noticeable toxicity was observed, even after 2 days of incubation. Intriguingly, the cell viability was further enhanced as the incubation time increased, suggesting the capability of the MOF-801 NPs to be utilized as cryopreservation nanoagents for both normal and cancer cells.[36] The cell viability was also explored according to the concentration of the MOF NPs (Figure S14). For reference, DMSO is widely used as a cryopreservation agent.[18] However, it induces high cytotoxicity at higher concentrations, thereby impacting cell survivability. Specifically, Yuan et al. reported that 5% (v/v) DMSO at a concentration of 5% (v/v) in Dulbecco's modified Eagle medium (DMEM) containing 10% (v/v) fetal bovine serum (FBS) causes a 40% decrease in cell density and 32% decrease in cell viability, which are considered lethal.[20] On the other hand, the developed MOF-801 NP 10 nm exhibited extremely good cell viability even at a high concentration (up to ~400 μg/mL, Figure S14). The cell viability tended to improve as the concentration increased, indicating that MOF-801 NPs are not toxic in the cellular environment.

Driven by the above results, the MOF-801 NPs were tested for the cryopreservation of the 293T cells compared to DMSO.[55−57] We investigated the cellular uptake and intra-

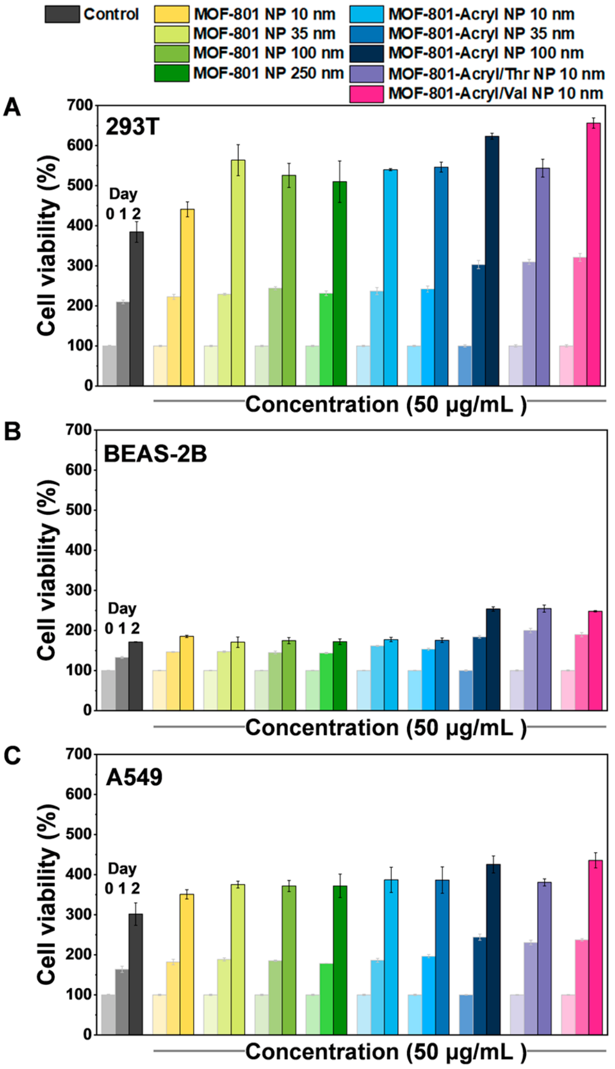

Figure 4. Cell viability of (A) 293T, (B) BEAS-2B, and (C) A549 treated with various MOF-801 NPs (50 μg/mL) for 1 and 2 days, determined by CellTiter-Glo 3D assay. The cell viability (%) represents the percent of viable cells after exposure to MOF-801 NPs, with respect to the control (100%). The data represent the mean and standard deviation of five independent samples.

cellular distribution of MOF-801 NPs. DMSO can penetrate the cell to reduce the electrolyte concentration of the remaining unfrozen solution inside and around the cell, resulting in minimizing cell damage. Consequently, intracellular ice growth, osmotic shock, and cell shrinkage are reduced.[55,58,59] Internalization of bare MOF-801 NPs and Val- and Thr-functionalized MOF-801 NPs into 293T cells was confirmed by flow cytometry and confocal laser scanning microscopy (CLSM) (Figures 5, S15, and S16).[59] We exposed cells to acridine orange-labeled MOF-NPs for 24 h. As shown in Figures 5A and S15, it was confirmed by flow cytometry analysis that all the bare MOF-801 NPs, MOF- 801-Acryl/Val, and/Thr NPs with sizes of 10 and 100 nm were successfully internalized into the cells. This was consistent with the CLSM images (Figures 5B and S16). The 293T cells treated with free acridine orange showed no green fluorescence in the cells indicative of no cellular uptake (Figure 5B, upper). In contrast, the MOF-801 NPs with green fluorescence can be seen in the cytoplasm of 293T cells (Figure 5B, bottom). These results indicate that the MOF-801 NPs would be a promising cryopreservative that could replace DMSO, so cryopreservation for the 293T cell line proceeded.

Post-thaw Cell Recovery and Proliferation Efficacy of MOF NP Cryopreservatives

To assess the cryopreservation effect of each MOF-801 NP with or without surface-functionalization, the number of 293T cells recovered and cultured after cell freezing/thawing was identified (Figures 6 and S17).[55,57] The 293T cells were treated and incubated with 50 μg/mL of MOF-801 NP solution, followed by a freezing/thawing protocol (see the Supporting Information). The cryopreserved MOF NPs-treated cells showed an intact morphology with an elongated spindle shape even at 24 and 48 h post-thaw (Figure 6A–E). The post-thaw cell recovery rate was calculated by the ratio of the number of cells recovered with intact membranes to the total number of frozen cells (Figures 6F and S17).[60,61] Notably, the smaller-sized MOF NPs showed higher efficacy as cryopreservatives, similar to the tendency shown with regard to the IRI effect. When 10 and 100 nm NPs were compared, the former exhibited a 9.2% better cell recovery rate. Furthermore, the MOF-801-Acryl NPs showed a recovery rate almost similar to the bare MOF-801 NPs; namely, 12.3% of the cells were recovered after treatment with the MOF-801-Acryl NPs 10 nm, while 18.0% were recovered with MOF-801 NPs 10 nm. As expected, when the test cells were cryopreserved with the surface-functionalized MOF NPs using amino acids, the MOF-801-Acryl/Val NPs and MOF-801-Acryl/Thr NPs enabled more cells to be recovered with intact membranes to be recovered with the rates of 54.9 and 62.8%, respectively. A live/dead assay of recovered cells was performed.[60,61] Most of the cells treated with the MOF NP solutions were viable with approximately 95% post-thaw cell viability, which was estimated by dividing the number of live cells by the sum of the number of live and dead cells (Figure 6D). These results restated that the size-controlled MOF-801-Acryl NPs effectively introduced ice-binding amino acids found in natural AFPs (Val and Thr) on their surface via surface-functionalization, to achieve a size-dependent antifreeze effect for the cryopreservation of cells. The antifreeze effect can be further enhanced with the reproduced duality of hydrophilic and hydrophobic interactions. The vitality of the recovered cells was investigated through a proliferation test (Figure 6G,H). Compared with DMSO 10% (v/v)-treated cells that increased 10.7-fold at 96 h post-thaw, cells treated with MOF NPs 10 nm increased 9.3-fold on average. After cryopreservation using MOF NP solutions, the cell proliferation capability showed a significant effect, comparable to that of the control. Such cryopreservation capability of MOF-801 NPs was further verified with the A549 cells (Figure S18); namely, MOF-801-Acryl/Val and Thr NPs 10 nm showed high recovery rates of 61.5% and 68.3%, respectively (Figure S18B), with an approximately 9.8-fold increase in cell number at 96 h post-thaw (Figure S18C). Although the post-thaw cell recovery rate of MOF-801 NPs is slightly lower than that of DMSO 10% (v/v), as mentioned above, MOF NPs showed good biocompatibility regardless of concentration, unlike the cytotoxicity exhibited by DMSO. Therefore, this research outcome highlighted the favorable applicability of our developed MOF NPs in practical cellular cryopreservation.

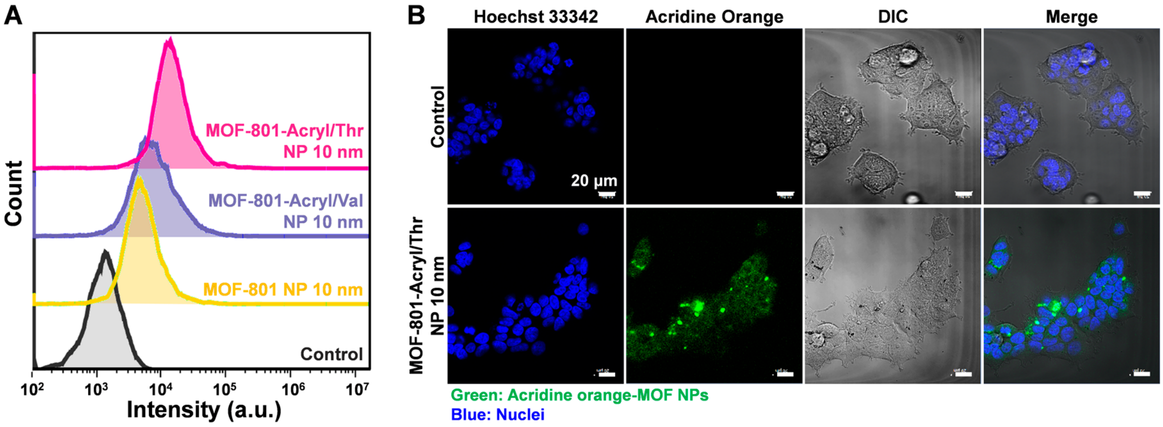

Figure 5. (A) Stacked flow cytometry histograms of 293T cells incubated with acridine orange tagged MOF-801 NP, MOF-801-Acryl/Val NP, and MOF-801-Acryl/Thr NP 10 nm (50 μg/mL). (B) CLSM images of 293T cell nuclei treated with free acridine orange (upper) and uptake of MOF-801-Acryl/Thr NPs 10 nm (50 μg/mL) by 293T cells (bottom). NPs were tagged with acridine orange (green), and the cell nuclei were stained with Hoechst 33342 (blue).

CONCLUSIONS

In conclusion, we reported Zr-based MOF-801 NP agents with excellent biocompatibility for cell cryopreservation by aligning the ice-binding moieties of the NP surface with the lattice of the ice crystal plane and inducing the formation of micro-curvatures on the ice surface. This led to an excellent IRI effect through thermodynamic control of clathrate water anchored on the ice surface, thereby resulting in an excellent cell recovery rate after freezing/thawing. This study proposed a feasible strategy for developing effective, biocompatible, and mass-producible low-cost cell cryopreservation nanoagents based on the characteristics of IBPs. Using the ability of MOFs to diversify the metal and ligands, we can change critical factors such as lattice parameters, size, and shape of MOF NPs to facilitate the development of soft materials with antifreeze capability.

METHODS

Materials

Solvents and all other chemicals were purchased and used as received unless otherwise noted. *N,N*-Dimethylformamide (DMF), methanol, ethanol, and formic acid (reagent grade, ≥99.0%) were obtained from Samchun Chemical Co., Ltd. (Seoul, Republic of Korea). Zirconyl chloride octahydrate ($ZrOCl_2·8H_2O$, reagent grade, ≥98.0%), fumaric acid (≥99.0%), and 2-carboxyethyl acrylate were purchased from Sigma-Aldrich Chemical Co., Ltd. (St. Louis, MO, USA). L-Val (high pressure liquid chromatography (HPLC) grade, ≥98%) and L-Thr (HPLC grade, ≥98%) were also purchased from Sigma-Aldrich Chemical Co., Ltd. Deionized water (DI water) of Milli-Q water with a resistivity of 18.2 MΩ·cm was obtained from a Millipore RiOs/Origin water purification system (Burlington, MA, USA). The 293T, BEAS-2B, and A549 cells were purchased from American Type Culture Collection (ATCC, Manassas, VA, USA). The DMEM, FBS, 1% penicillin/streptomycin, PBS, and DMSO were purchased from Corning (Corning, NY, USA). CellTiter-Glo Luminescent Cell viability Assay Kit and GloMax 96 Microplate Luminometer were obtained from Promega (Madison, WI, USA). Acridine orange, poly(vinyl alcohol) mounting medium with DABCO, hemocytometers, trypan blue solution, and ethylenediaminetetraacetic acid (EDTA) were acquired from Sigma-Aldrich Chemical Co., Ltd. Hoechst 33342 and LIVE/DEAD Viability/Cytotoxicity kit were purchased from Thermo Fisher Scientific (Waltham, MA, USA). DMSO-d_6 was purchased from Cambridge isotope laboratories, Inc. (Tewksbury, MA, USA).

Syntheses

Synthesis of MOF-801 NPs (10 nm). MOF-801 NPs were synthesized following the previously reported methods with some modifications according to the NP size.[62] Briefly, 0.36 g of fumaric acid and 1.00 g of $ZrOCl_2·8H_2O$ were dissolved in 50 mL of DMF and 3.51 mL of formic acid. The mixture was heated at 120 °C for 16 h. Rounded-octahedral white crystals were collected and dispersed in ethanol (30 mL) under sonication and magnetic stirring for 24 h at room temperature and subsequently washed 3 times with ethanol. Then, the products were collected by centrifugation and dried at 100 °C for 3 h to yield an activated sample. Syntheses of MOF-801 NPs with different sizes (35, 100, and 250 nm) are detailed in the Supporting Information.

Synthesis of MOF-801-Acryl NPs (10, 35, and 100 nm). The amounts of 3.5 g of MOF-801 NPs and 0.5 g of 2-carboxyethyl acrylate were dissolved in 40 mL of ethanol. The resulting mixtures were stirred at 50 °C for 16 h. As-synthesized MOF-801-Acryl NPs were acquired via centrifugation and then dispersed in ethanol (100 mL) under sonication and magnetic stirring for 24 h at room temperature and subsequently washed 3 times with ethanol. Then, the products were dried at 100 °C for 3 h to yield an activated sample.

Synthesis of MOF-801-Acryl/Val NPs and MOF-801-Acryl/Thr NPs (10, 35, and 100 nm). Here, 400 μmol of L-Val or L-Thr was completely dissolved in 10 mL of ethanol. Then, 2 mg of MOF-801-Acryl NPs 10, 35, and 100 nm were added, respectively. Sonication was performed for 30 min so that each compound and MOF-801-Acryl NPs were sufficiently dispersed in the solvent, and then vigorously stirred at room temperature for 24 h to allow the aza-Michael addition reaction[63] between the MOF-801-Acryl NP 10, 35, and 100 nm and each amino acid. The functionalized MOF-801-Acryl/Val NPs and MOF-801-Acryl/Thr NPs were acquired via centrifugation and then dispersed in DI water under sonication. After centrifugation at 4000 rpm for 15 min, washing was performed 3 times in DI water, then MOF NPs were dispersed in ethanol once again, magnetic stirring was performed for 24 h at room temperature, and subsequently washed 3 times. Whether all residual free amino acids were removed was confirmed through the ninhydrin test.[64] The remaining solvents after synthesis was evaporated overnight in a vacuum state. The introduction of Val and Thr onto the surface of the MOF-801-Acryl NPs was confirmed to be successful by FT-IR spectroscopy and XPS.

Generally, after the synthesis of MOF-801 NPs, the MOF NPs were collected and dispersed in ethanol and subsequently washed with ethanol 3 times at least. In particular, the successful removal of free amino acids from the amino acid-conjugated MOF-801-Acryl NP was confirmed with the ninhydrin test (insets of Figure S6).[64] The free amino acid can provide ammonia through oxidative deamination

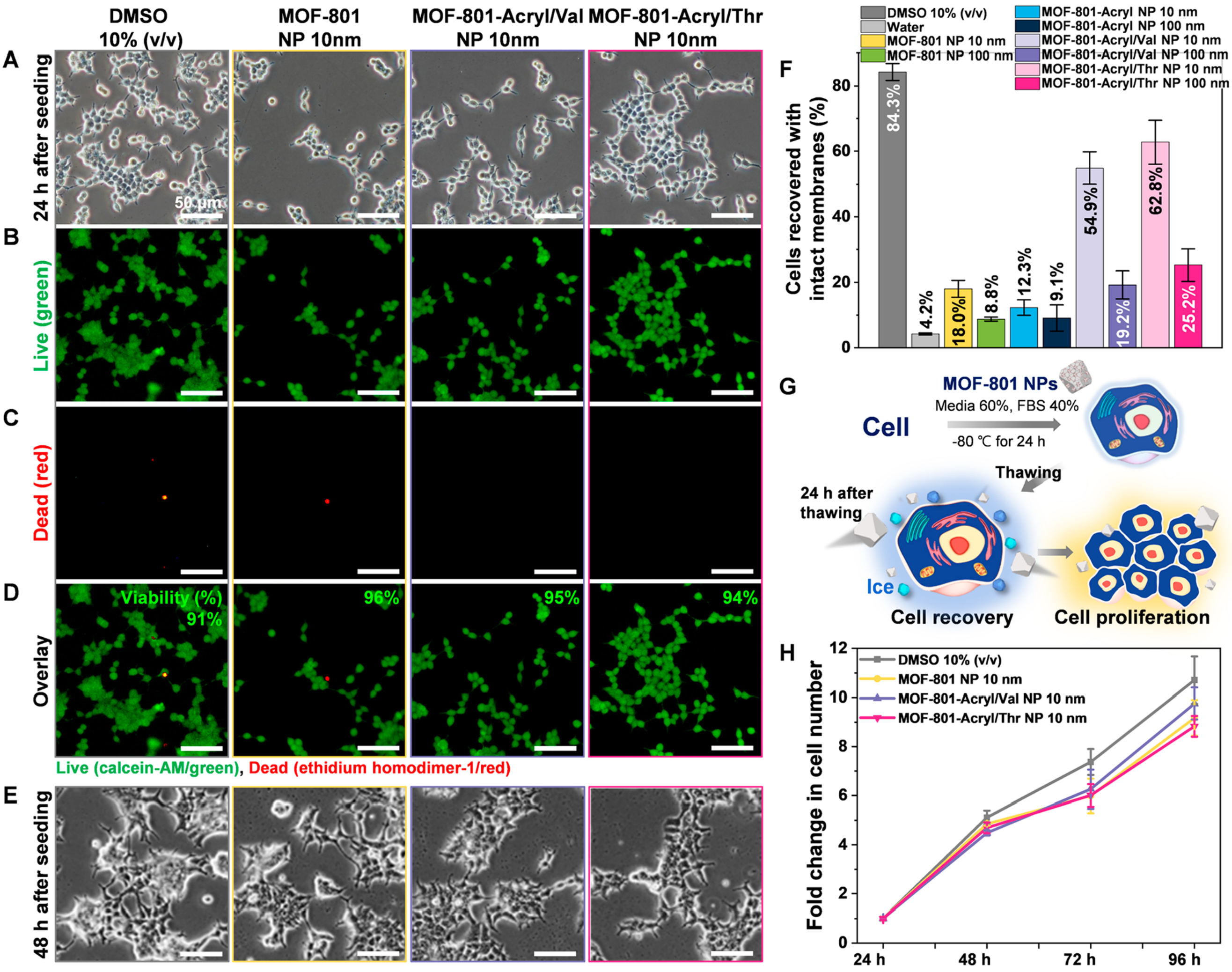

Figure 6. (A) Bright-field and (B−D) fluorescence microscopic images of 293T cells treated with DMSO 10% (v/v), MOF-801 NP 10 nm, MOF-801-Acryl/Val NP 10 nm, and MOF-801-Acryl/Thr NP 10 nm solutions after freezing/thawing and seeding for 24 h. (B−D) Live/dead staining of 293T cells showing 24 h post-thaw cell viability. (B) Live cells were stained with calcein-AM (green fluorescence), and (C) dead cells were stained with ethidium homodimer-1 (red fluorescence). (D) The live/dead images were overlaid, and the cell viability (%) was calculated. (E) Bright-field microscopic images of 293T cells after 48 h post-thaw. (F) Representative graph showing 24 h post-thaw cell recovery rate of 10% (v/v) DMSO and MOF-801 NPs determined by trypan blue exclusion assay. A solution composed of 60% (v/v) media and 40% (v/v) FBS was used. The error bars represent the standard deviation from the three individual experiments. (G) Schematic illustration showing the proposed freezing/thawing process for cell cryopreservation by MOF-801 NPs. (H) Proliferation curves of the cryopreserved 293T cells from 24 to 96 h after freezing/thawing. The error bars represent the standard deviation from the four individual experiments.

when exposed to ninhydrin, and subsequently react with another ninhydrin, resulting in the formation of diketohydrin. This complex shows an intense blue color. MOF-801-Acryl/Val and/Thr NPs did not show a blue color as a result of the ninhydrin test, which means there are no remaining free amino acids in the MOF NPs-dispersed.

IRI Analysis

IRI was measured using a "splat" assay, as reported in the literature.[15] A volume of 10 μL of MOF NP dispersions in PBS solution (0.5 mg/mL) was prepared freshly before use and dropped from a height of 1.0 m onto the surface of a precooled (−150 °C) coverslip to make a thin film of ice. The glass coverslip with the ice thin film was transferred onto the cryo stage set at −20 °C. Then, the temperature of the glass coverslip was gradually increased to −6 °C at a rate of 5 min^{-1}, and the sample was held at −6 °C under N_2 for 30 min. Ten of the largest domains in the field of view were chosen and averaged to evaluate the IRI activity. Images were taken with 10 min intervals from the initial state to 30 min later. Image processing was conducted using *ImageJ*.[65] MLGS and standard deviation were averaged in three individual experiments.

Cellular Cryopreservation Capability of MOF-801 NPs

Cell Culture. The 293T, BEAS-2B, and A549 cell lines were cultured in DMEM containing 10% FBS and 1% penicillin/streptomycin. All cell lines were cultured at 37 °C in a humidified atmosphere of 5% CO_2 and air. Then, the cells were treated with 0.25% trypsin and 1 mM EDTA and removed from the adherent culture. The harvested cells were counted using the trypan blue exclusion assay.

Cell Viability Assay. The 293T, BEAS-2B, and A549 were seeded at 5 × 10^3 cells per 96 well white bottom culture plate with PBS as control and various concentrations of MOF-801 NP solution for 48 h. Cell viability was measured by CellTiter-Glo Luminescent Cell Viability Assay Kit according to the guidelines recommended. Briefly, 100 μL of CellTiter-Glo substrate in buffer reagent was added to each well and incubated for 10 min on the shaker and 10 min standing at room temperature. The luminescent signal was measured on a GloMax 96 Microplate Luminometer. Cytotoxicity was obtained by comparing the luminescent signal treated cells to that of control cells. All experiments were repeated five times independently.

Analysis of Cellular Uptake by CLSM. For demonstrating the cellular uptake of MOF-801 NPs, acridine orange was introduced to the MOF NPs̀ surface. Dispersions of MOF NPs in DI water (50 μg/mL) were incubated with acridine orange aqueous solution (5 μg/mL) overnight to induce hydrogen bonding between acridine orange and carboxylic acid groups on the MOF NPs̀ surface,[66] and then washed several times with DI water. 293T cells were seeded in a confocal slide at the density of 1×10^5 cells per well and 20 μL of MOF-801 NPs dispersion was added into the wells. The cells were treated with acridine orange tagged MOF-801 NPs for 24 h, mimicking the freezing/thawing protocol used later. Free acridine orange solution was prepared as a control. Cellular images of intracellular localization were obtained by an inverted CLSM. Images were obtained with the ZEN2009 software (Carl Zeiss, Oberkochen, Germany). To stain the nucleus, cells were stained with Hoechst 33342 (1 mg/mL) and rinsed 3 times with PBS. Cells were mounted in a poly(vinyl alcohol) mounting medium with DABCO.

Flow Cytometry Analysis. 293T cells were seeded in 12-well plates and treated with acridine orange tagged MOF-801 NPs dispersions (50 μg/mL) for 24 h. After that, the medium was removed, and cells were harvested with trypsin and then fixed with 4% paraformaldehyde and washed several times with PBS. The results are reported as the median of the distribution of cell fluorescence intensity obtained by analyzing 1×10^4 cells in the gate. The results are analyzed by Summit Software 6.0 (Beckman Coulter, CA, USA). Values of the internalization score, mean fluorescence intensity, and mean side scatter intensity were calculated for at least 5000 cells per sample.

Cryopreservation of 293T and A549 Cell Lines. To measure the cellular cryopreservation efficiency of MOF-801 NPs, freezing/thawing experiments were performed.[55,56] 293T cells were seeded at 4×10^6 cells per vial, and A549 cells were seeded at 2×10^6 cells per vial. The cells were put into a solution composed of 60% (v/v) media and 40% (v/v) FBS and 50 μg/mL MOF-801 NPs in total 500 μL volume. DI water and DMSO 10% (v/v) were set as the control groups. Then, it was stored for a day and frozen in a deep freezer at 1 °C min^{-1} to −80 °C for 24 h. Then, the frozen stock of cells was stored in a liquid N_2 tank for 24 h. The thawing process was carried out by incubating the frozen stock in a 37 °C water bath for 2 min. The cell freezing stock mixture was transferred in 4.5 mL of media in a 15 mL tube and centrifuged at 1000 rpm for 3 min. After the supernatant was removed, the cell pellets were suspended in 1 mL of complete media and seeded in 6-well plates. The seeded cells were incubated in a humidified atmosphere for 24 h and then treated with 0.25% trypsin and EDTA in a balanced salt solution to be dissociated.

Trypan Blue Exclusion Assay. The number of recovered cells with intact membranes was determined by trypan blue exclusion assay.[60] After freezing/thawing 293T and A549 cell lines, the cells were seeded and incubated for 24 h. Following the incubation, cell media was discarded to exclude nonattached cells in the assay, and cells were washed with PBS. The cells were treated with a 0.4% trypan blue solution and counted at 25 °C using a hemocytometer. The post-thaw cell recovery rate was calculated by eq 1 as shown below.[60]

$$\text{recovery}_{\text{trypan-blue-staining}}(\%) = \frac{\text{cells}_{\text{unstained}}}{\text{cells}_{\text{frozen}}} \times 100 \qquad (1)$$

Live/Dead Assay. To further confirm how many cells survived from freezing/thawing, we conducted a live/dead assay using 293T and A549 cell lines. After thawing the cells in a 35Ø glass-bottom dish and incubating for 24 h, the cells were washed with PBS. A live/dead solution was used as a purchase containing calcein-AM and ethidium homodimer-1. Calcein-AM of 5 μL and ethidium homodimer-1 of 20 μL in 10 mL of PBS was added, and the plate was incubated at room temperature for 30 min. After that, bright-field and fluorescence images were obtained at 530 and 645 nm on a fluorescence microscope. Live cells are stained with calcein-AM and show green fluorescence, and dead cells are stained with ethidium homodimer-1 and show red fluorescence. The image processing was conducted using *ImageJ*.[65] The post-thaw cell viability was calculated by eq 2 as shown below.[60]

$$\text{viability}_{\text{live/dead-assay}}(\%) = \frac{\text{cells}_{\text{green-fluorescence}}}{\text{cells}_{\text{green-fluorescence}} + \text{cells}_{\text{red-fluorescence}}} \times 100 \qquad (2)$$

Proliferation Test. Cryopreserved and recovered 293T and A549 cells were dissociated and counted. Cells were plated in 6-well plates at constant density. Cells were incubated at 37 °C in a humidified atmosphere of 5% CO and air until 96 h post-thaw and then dissociated using 0.25% trypsin and EDTA in a balanced salt solution for counting every 24 h.

■ ASSOCIATED CONTENT

Supporting Information

The Supporting Information is available free of charge at https://pubs.acs.org/doi/10.1021/jacsau.2c00562.

> Experimental methods including instruments, syntheses of MOF-801 NPs (35, 100, and 250 nm), detailed description of size-dependent IRI activity of MOF-801 NPs by Gibbs−Thomson effect, TEM images, FT-IR spectra, PXRD patterns, XPS spectra, cryomicroscopy images, cell viability, flow cytometry histograms, CLSM images, live/dead staining images, and MLGS values (PDF)

■ AUTHOR INFORMATION

Corresponding Authors

Eunji Lee − *School of Materials Science and Engineering, Gwangju Institute of Science and Technology (GIST), Gwangju 61005, Republic of Korea;* orcid.org/0000-0001-7494-1776; Email: eunjilee@gist.ac.kr

Peter C.W. Lee − *Department of Biomedical Sciences, Asan Medical Center, University of Ulsan College of Medicine, Seoul 05505, Republic of Korea;* orcid.org/0000-0002-2320-6365; Email: pclee@amc.seoul.kr

Hee Jung Lee − *Composites Research Division, Korea Institute of Materials Science (KIMS), Changwon 51508, Republic of Korea;* Email: hj0889@kims.re.kr

Authors

Nayeong Jeon − *School of Materials Science and Engineering, Gwangju Institute of Science and Technology (GIST), Gwangju 61005, Republic of Korea;* orcid.org/0000-0002-2869-1611

In-ho Jeong − *Department of Biomedical Sciences, Asan Medical Center, University of Ulsan College of Medicine, Seoul 05505, Republic of Korea*

Eunyeong Cho − *Composites Research Division, Korea Institute of Materials Science (KIMS), Changwon 51508, Republic of Korea*

Ilhyung Choi − *School of Materials Science and Engineering, Gwangju Institute of Science and Technology (GIST), Gwangju 61005, Republic of Korea;* orcid.org/0000-0002-7372-8815

Jiyeon Lee − *School of Materials Science and Engineering, Gwangju Institute of Science and Technology (GIST), Gwangju 61005, Republic of Korea*

Eun Hee Han − *Research Center for Bioconvergence Analysis, Korea Basic Science Institute (KBSI), Cheongju 28119, Republic of Korea*

Complete contact information is available at:
https://pubs.acs.org/10.1021/jacsau.2c00562

Author Contributions

The manuscript was written through the contributions of all authors.

Notes

The authors declare no competing financial interest.

■ ACKNOWLEDGMENTS

This research was supported by Basic Science Research Program (2022R1A2C2012889) and Creative Materials Discovery Program (2017M3D1A1039421) through the National Research Foundation of Korea (NRF) funded by the Ministry of Science and ICT. This research was also supported by the "Practical Research and Development support program supervised by the GIST Technology Institute (GTI)" grant funded by GIST in 2022, the Fundamental Research Program (PNK 8070) of the Korea Institute of Materials Science (KIMS), and the Korea Drug Development Fund by the Ministry of Science and ICT, the Ministry of Trade, Industry, and Energy, and the Ministry of Health and Welfare (HN21C1078).

■ REFERENCES

(1) DeVries, A. L.; Wohlschlag, D. E. Freezing Resistance in Some Antarctic Fishes. *Science* **1969**, *163*, 1073−1075.

(2) Liou, Y. C.; Tocilj, A.; Davies, P. L.; Jia, Z. Mimicry of Ice Structure by Surface Hydroxyls and Water of a β-Helix Antifreeze Protein. *Nature* **2000**, *406*, 322−324.

(3) Robles, V.; Valcarce, D. G.; Riesco, M. F. The Use of Antifreeze Proteins in the Cryopreservation of Gametes and Embryos. *Biomolecules* **2019**, *9*, 181.

(4) Hirano, Y.; Nishimiya, Y.; Matsumoto, S.; Matsushita, M.; Todo, S.; Miura, A.; Komatsu, Y.; Tsuda, S. Hypothermic Preservation Effect on Mammalian Cells of Type III Antifreeze Proteins from Notched-Fin Eelpout. *Cryobiology* **2008**, *57*, 46−51.

(5) Heisig, M.; Abraham, N. M.; Liu, L.; Neelakanta, G.; Mattessich, S.; Sultana, H.; Shang, Z.; Ansari, J. M.; Killiam, C.; Walker, W.; Cooley, L.; Flavell, R. A.; Agaisse, H.; Fikrig, E. Antivirulence Properties of an Antifreeze Protein. *Cell Rep* **2014**, *9*, 417−424.

(6) Ustun, N. S.; Turhan, S. Antifreeze Proteins: Characteristics, Function, Mechanism of Action, Sources and Application to Foods. *J. Food Process. Preserv* **2015**, *39*, 3189−3197.

(7) Graham, B.; Bailey, T. L.; Healey, J. R. J.; Marcellini, M.; Deville, S.; Gibson, M. I. Polyproline as a Minimal Antifreeze Protein Mimic That Enhances the Cryopreservation of Cell Monolayers. *Angew. Chem. Int. Ed* **2017**, *56*, 15941−15944.

(8) Georgiou, P. G.; Marton, H. L.; Baker, A. N.; Congdon, T. R.; Whale, T. F.; Gibson, M. I. Polymer Self-Assembly Induced Enhancement of Ice Recrystallization Inhibition. *J. Am. Chem. Soc.* **2021**, *143*, 7449−7461.

(9) Kristiansen, E.; Zachariassen, K. E. The Mechanism by Which Fish Antifreeze Proteins Cause Thermal Hysteresis. *Cryobiology* **2005**, *51*, 262−280.

(10) Garnham, C. P.; Campbell, R. L.; Davies, P. L. Anchored Clathrate Waters Bind Antifreeze Proteins to Ice. *Proc. Natl. Acad. Sci. U. S. A* **2011**, *108*, 7363−7367.

(11) Haymet, A. D. J.; Ward, L. G.; Harding, M. M. Winter Flounder "Antifreeze" Proteins: Synthesis and Ice Growth Inhibition of Analogues That Probe the Relative Importance of Hydrophobic and Hydrogen-Bonding Interactions. *J. Am. Chem. Soc.* **1999**, *121*, 941−948.

(12) Zachariassen, K. E.; Husby, J. A. Antifreeze Effect of Thermal Hysteresis Agents Protects Highly Supercooled Insects. *Nature* **1982**, *298*, 865−867.

(13) Murray, K. A.; Gibson, M. I. Chemical Approaches to Cryopreservation. *Nat. Rev. Chem.* **2022**, *6*, 579−593.

(14) Knight, C. A.; De Vries, A. L.; Oolman, L. D. Fish Antifreeze Protein and the Freezing and Recrystallization of Ice. *Nature* **1984**, *308*, 295−296.

(15) Knight, C. A.; Wen, D.; Laursen, R. A. Nonequilibrium Antifreeze Peptides and the Recrystallization of Ice. *Cryobiology* **1995**, *32*, 23−34.

(16) Knight, C. A.; Hallett, J.; DeVries, A. L. Solute Effects on Ice Recrystallization: An Assessment Technique. *Cryobiology* **1988**, *25*, 55−60.

(17) Ashwood-Smith, M. J.; Friedmann, G. B. Lethal and Chromosomal Effects of Freezing, Thawing, Storage Time, and x-Irradiation on Mammalian Cells Preserved at −196° in Dimethyl Sulfoxide. *Cryobiology* **1979**, *16*, 132−140.

(18) Jacob, S. W.; de la Torre, J. C. Pharmacology of Dimethyl Sulfoxide in Cardiac and CNS Damage. *Pharmacol. Reports* **2009**, *61*, 225−235.

(19) Asghar, W.; El Assal, R.; Shafiee, H.; Anchan, R. M.; Demirci, U. Preserving Human Cells for Regenerative, Reproductive, and Transfusion Medicine. *Biotechnol. J.* **2014**, *9*, 895−903.

(20) Yuan, C.; Gao, J.; Guo, J.; Bai, L.; Marshall, C.; Cai, Z.; Wang, L.; Xiao, M. Dimethyl Sulfoxide Damages Mitochondrial Integrity and Membrane Potential in Cultured Astrocytes. *PLoS One* **2014**, *9*, No. e107447.

(21) Iwatani, M.; Ikegami, K.; Kremenska, Y.; Hattori, N.; Tanaka, S.; Yagi, S.; Shiota, K. Dimethyl Sulfoxide Has an Impact on Epigenetic Profile in Mouse Embryoid Body. *Stem Cells* **2006**, *24*, 2549−2556.

(22) Kawai, K.; Li, Y. S.; Song, M. F.; Kasai, H. DNA Methylation by Dimethyl Sulfoxide and Methionine Sulfoxide Triggered by Hydroxyl Radical and Implications for Epigenetic Modifications. *Bioorg. Med. Chem. Lett.* **2010**, *20*, 260−265.

(23) Qin, Q.; Zhao, L.; Liu, Z.; Liu, T.; Qu, J.; Zhang, X.; Li, R.; Yan, L.; Yan, J.; Jin, S.; Wang, J.; Qiao, J. Bioinspired l -Proline Oligomers for the Cryopreservation of Oocytes via Controlling Ice Growth. *ACS Appl. Mater. Interfaces* **2020**, *12*, 18352−18362.

(24) Choi, J.; Kim, S.; Yoo, J.; Choi, S. H.; Char, K. Self-Healable Antifreeze Hydrogel Based on Dense Quadruple Hydrogen Bonding. *Macromolecules* **2021**, *54*, 6389−6399.

(25) Stevens, C. A.; Bachtiger, F.; Kong, X. D.; Abriata, L. A.; Sosso, G. C.; Gibson, M. I.; Klok, H. A. A Minimalistic Cyclic Ice-Binding Peptide from Phage Display. *Nat. Commun.* **2021**, *12*, 2675.

(26) Biggs, C. I.; Stubbs, C.; Graham, B.; Fayter, A. E. R.; Hasan, M.; Gibson, M. I. Mimicking the Ice Recrystallization Activity of Biological Antifreezes. When Is a New Polymer "Active"? *Macromol. Biosci* **2019**, *19*, 1900082.

(27) Ploetz, E.; Engelke, H.; Lächelt, U.; Wuttke, S. The Chemistry of Reticular Framework Nanoparticles: MOF, ZIF, and COF Materials. *Adv. Funct. Mater.* **2020**, *30*, 1909062.

(28) Andreo, J.; Ettlinger, R.; Zaremba, O.; Peña, Q.; Lächelt, U.; De Luis, R. F.; Freund, R.; Canossa, S.; Ploetz, E.; Zhu, W.; Diercks, C. S.; Gröger, H.; Wuttke, S. Reticular Nanoscience: Bottom-Up Assembly Nanotechnology. *J. Am. Chem. Soc.* **2022**, *144*, 7531−7550.

(29) Furukawa, H.; Gándara, F.; Zhang, Y. B.; Jiang, J.; Queen, W. L.; Hudson, M. R.; Yaghi, O. M. Water Adsorption in Porous Metal-Organic Frameworks and Related Materials. *J. Am. Chem. Soc.* **2014**, *136*, 4369−4381.

(30) Kim, H.; Yang, S.; Rao, S. R.; Narayanan, S.; Kapustin, E. A.; Furukawa, H.; Umans, A. S.; Yaghi, O. M.; Wang, E. N. Water Harvesting from Air with Metal-Organic Frameworks Powered by Natural Sunlight. *Science* **2017**, *356*, 430−434.

(31) Fischer, S.; Roeser, J.; Lin, T. C.; DeBlock, R. H.; Lau, J.; Dunn, B. S.; Hoffmann, F.; Fröba, M.; Thomas, A.; Tolbert, S. H. A Metal−Organic Framework with Tetrahedral Aluminate Sites as a Single-Ion Li+ Solid Electrolyte. *Angew. Chem. Int. Ed* **2018**, *57*, 16683−16687.

(32) Zhou, S.; Shekhah, O.; Jia, J.; Czaban-Jóźwiak, J.; Bhatt, P. M.; Ramírez, A.; Gascon, J.; Eddaoudi, M. Electrochemical Synthesis of

Continuous Metal−Organic Framework Membranes for Separation of Hydrocarbons. *Nat. Energy* **2021**, *6*, 882−891.

(33) Wu, C.; Zhang, K.; Wang, H.; Fan, Y.; Zhang, S.; He, S.; Wang, F.; Tao, Y.; Zhao, X.; Zhang, Y. B.; Ma, Y.; Lee, Y.; Li, T. Enhancing the Gas Separation Selectivity of Mixed-Matrix Membranes Using a Dual-Interfacial Engineering Approach. *J. Am. Chem. Soc.* **2020**, *142*, 18503−18512.

(34) Hou, S. L.; Dong, J.; Jiang, X. L.; Jiao, Z. H.; Zhao, B. A Noble-Metal-Free Metal−Organic Framework (MOF) Catalyst for the Highly Efficient Conversion of CO 2 with Propargylic Alcohols. *Angew. Chem. Int. Ed* **2019**, *58*, 577−581.

(35) Yang, B.; Ding, L.; Yao, H.; Chen, Y.; Shi, J. A Metal-Organic Framework (MOF) Fenton Nanoagent-Enabled Nanocatalytic Cancer Therapy in Synergy with Autophagy Inhibition. *Adv. Mater.* **2020**, *32*, 1907152.

(36) Zhu, W.; Guo, J.; Agola, J. O.; Croissant, J. G.; Wang, Z.; Shang, J.; Coker, E.; Motevalli, B.; Zimpel, A.; Wuttke, S.; Brinker, C. J. Metal-Organic Framework Nanoparticle-Assisted Cryopreservation of Red Blood Cells. *J. Am. Chem. Soc.* **2019**, *141*, 7789−7796.

(37) Wißmann, G.; Schaate, A.; Lilienthal, S.; Bremer, I.; Schneider, A. M.; Behrens, P. Modulated Synthesis of Zr-Fumarate MOF. *Microporous Mesoporous Mater.* **2012**, *152*, 64−70.

(38) Ganesh, M.; Hemalatha, P.; Peng, M. M.; Cha, W. S.; Jang, H. T. Zr-Fumarate MOF a Novel CO2-Adsorbing Material: Synthesis and Characterization. *Aerosol Air Qual. Res.* **2014**, *14*, 1605−1612.

(39) Aswin Kumar, I.; Naushad, M.; Ahamad, T.; Viswanathan, N. Facile Fabrication of Tunable Porous Zirconium Fumarate Based Metal Organic Frameworks in the Retention of Nutrients from Water. *Environ. Sci. Water Res. Technol.* **2020**, *6*, 2856−2870.

(40) Ren, J.; Musyoka, N. M.; Langmi, H. W.; Walker, J.; Mathe, M.; Liao, S. In-Situ IR Monitoring to Probe the Formation of Structural Defects in Zr-Fumarate Metal−Organic Framework (MOF). *Polyhedron* **2018**, *153*, 205−212.

(41) Reznik, D.; Olk, C. H.; Neumann, D. A.; Copley, J. R. D. X-Ray Powder Diffraction from Carbon Nanotubes and Nanoparticles. *Phys. Rev. B* **1995**, *52*, 116−124.

(42) Liu, L.; Qiao, Z.; Cui, X.; Pang, C.; Liang, H.; Xie, P.; Luo, X.; Huang, Z.; Zhang, Y.; Zhao, Z. Amino Acid Imprinted UiO-66s for Highly Recognized Adsorption of Small Angiotensin-Converting-Enzyme-Inhibitory Peptides. *ACS Appl. Mater. Interfaces* **2019**, *11*, 23039−23049.

(43) Drori, R.; Davies, P. L.; Braslavsky, I. Experimental Correlation between Thermal Hysteresis Activity and the Distance between Antifreeze Proteins on an Ice Surface. *RSC Adv.* **2015**, *5*, 7848−7853.

(44) Zhang, Z.; Liu, X. Y. Control of Ice Nucleation: Freezing and Antifreeze Strategies. *Chem. Soc. Rev.* **2018**, *47*, 7116−7139.

(45) Chiu, C. C.; Shieh, F. K.; Tsai, H. H. G. Ligand Exchange in the Synthesis of Metal-Organic Frameworks Occurs Through Acid-Catalyzed Associative Substitution. *Inorg. Chem.* **2019**, *58*, 14457−14466.

(46) Yao, C. S.; Lei, S.; Wang, C. H.; Yu, C. X.; Shao, Q. Q.; Tu, S. J. One-Pot Three-Component Solvent-Free Synthesis of Benzo[4,5]-Imidazo[1,2-a] Pyrimidine Derivatives Catalyzed by Sulfamic Acid. *Chin. J. Chem.* **2008**, *26*, 2107−2111.

(47) Ding, M.; Jiang, H. L. Improving Water Stability of Metal−Organic Frameworks by a General Surface Hydrophobic Polymerization. *CCS Chem.* **2021**, *3*, 2740−2748.

(48) Warren, M. T.; Galpin, I.; Bachtiger, F.; Gibson, M. I.; Sosso, G. C. Ice Recrystallization Inhibition by Amino Acids: The Curious Case of Alpha- and Beta-Alanine. *J. Phys. Chem. Lett.* **2022**, *13*, 2237−2244.

(49) Isakov, A. I.; Lorenz, H.; Zolotarev, A. A.; Kotelnikova, E. N. Heteromolecular Compounds in Binary Systems of Amino Acids with Opposite and Same Chiralities. *CrystEngComm* **2020**, *22*, 986−997.

(50) McGrath, D. T.; Ryan, M. D.; Macinnis, J. J.; Vandenboer, T. C.; Young, C. J.; Katz, M. J. Selective Decontamination of the Reactive Air Pollutant Nitrous Acid: Via Node-Linker Cooperativity in a Metal-Organic Framework. *Chem. Sci.* **2019**, *10*, 5576−5581.

(51) Ding, Z.; Wang, C.; Zhou, B.; Su, M.; Yang, S.; Li, Y.; Qu, C.; Liu, H. Antifreezing Hydroxyl Monolayer of Small Molecules on a Nanogold Surface. *Nano Lett.* **2022**, *22*, 5307−5315.

(52) Etter, M. C. A New Role for Hydrogen-Bond Acceptors in Influencing Packing Patterns of Carboxylic Acids and Amides. *J. Am. Chem. Soc.* **1982**, *104*, 1095−1096.

(53) Perry, M. R.; Ebrahimi, T.; Morgan, E.; Edwards, P. M.; Hatzikiriakos, S. G.; Schafer, L. L. Catalytic Synthesis of Secondary Amine-Containing Polymers: Variable Hydrogen Bonding for Tunable Rheological Properties. *Macromolecules* **2016**, *49*, 4423−4430.

(54) Liu, K.; Wang, C.; Ma, J.; Shi, G.; Yao, X.; Fang, H.; Song, Y.; Wang, J. Janus Effect of Antifreeze Proteins on Ice Nucleation. *Proc. Natl. Acad. Sci. U. S. A* **2016**, *113*, 14739−14744.

(55) Tomás, R. M. F.; Bailey, T. L.; Hasan, M.; Gibson, M. I. Extracellular Antifreeze Protein Significantly Enhances the Cryopreservation of Cell Monolayers. *Biomacromolecules* **2019**, *20*, 3864−3872.

(56) Chang, T.; Zhao, G. Ice Inhibition for Cryopreservation: Materials, Strategies, and Challenges. *Adv. Sci.* **2021**, *8*, 2002425.

(57) Zhao, J.; Johnson, M. A.; Fisher, R.; Burke, N. A. D.; Stöver, H. D. H. Synthetic Polyampholytes as Macromolecular Cryoprotective Agents. *Langmuir* **2019**, *35*, 1807−1817.

(58) Mazur, P. Cryobiology: The Freezing of Biological Systems. *Science* **1970**, *168*, 939−949.

(59) Yao, X.; Jovevski, J. J.; Todd, M. F.; Xu, R.; Li, Y.; Wang, J.; Matosevic, S. Nanoparticle-Mediated Intracellular Protection of Natural Killer Cells Avoids Cryoinjury and Retains Potent Antitumor Functions. *Adv. Sci.* **2020**, *7*, 1902938.

(60) Murray, K. A.; Gibson, M. I. Post-Thaw Culture and Measurement of Total Cell Recovery Is Crucial in the Evaluation of New Macromolecular Cryoprotectants. *Biomacromolecules* **2020**, *21*, 2864−2873.

(61) Bailey, T. L.; Stubbs, C.; Murray, K.; Tomás, R. M. F.; Otten, L.; Gibson, M. I. Synthetically Scalable Poly(Ampholyte) Which Dramatically Enhances Cellular Cryopreservation. *Biomacromolecules* **2019**, *20*, 3104−3114.

(62) Kim, J. H.; Park, H. W.; Koo, S.-J.; Lee, D.; Cho, E.; Kim, Y.-K.; Shin, M.; Choi, J. W.; Lee, H. J.; Song, M. High Efficiency and Stable Solid-State Fiber Dye-Sensitized Solar Cells Obtained Using TiO_2 Photoanodes Enhanced with Metal Organic Frameworks. *J. Energy Chem.* **2022**, *67*, 458−466.

(63) Zou, B.; Jiang, H.-F. Synthesis of β -Amino Acids via Catalyst- and Solvent-Free Aza-Michael Reaction. *Chin. J. Chem.* **2008**, *26*, 1309−1314.

(64) Friedman, M.; Sigel, C. W. A Kinetic Study of the Ninhydrin Reaction. *Biochemistry* **1966**, *5*, 478−485.

(65) Schneider, C. A.; Rasband, W. S.; Eliceiri, K. W. NIH Image to ImageJ: 25 Years of Image Analysis. *Nat. Methods* **2012**, *9*, 671−675.

(66) Karmakar, A.; Banerjee, S.; Singh, B.; Mandal, N. C. Study of Hydrogen Bonding Interaction of Acridine Orange with Different Acceptor Molecules by Spectroscopic, Theoretical, and Antimicrobial Studies. *J. Mol. Struct.* **2019**, *1177*, 418−429.